Multi-Objective Optimization Design of Surface Mount Permanent Magnet Synchronous Motor for UAV

Xin-hao Tang, Gui-chang Zhang*, Wei-bin Huo, and Qian-qiang Zhang

School of Aeronautical Engineering, Civil Aviation University of China, Tianjin, 300300, China

(Received 6 May 2025, Received in final form 30 June 2025, Accepted 30 June 2025)

In order to address the vibration noise generated during the operation of the drone due to the operation of the motor, this paper selects the key structural parameters inside the motor as the optimization variables, and uses the average output torque, torque ripple and load air gap magnetic density as the optimization objectives for multi-objective optimization design. First, the excitation source of the motor vibration, the electromagnetic force, was analyzed analytically. At the same time, the main factor causing motor vibration, the radial electromagnetic force, and the vibration noise characteristics under different working conditions and speeds were simulated using finite element analysis. The source and spatial order distribution of the electromagnetic force and the vibration noise characteristics under multiple speeds were analyzed. Next, a response surface modeling (RSM) model, to solve the specific analytical relationship between the design variables and the optimization objectives, and to perform multi-objective optimization design of the motor by combining the Taguchi method improved by fuzzy theory. Then, a sensitivity analysis of each design variable is performed based on the Pearson coefficient, and different methods are used to perform secondary parameter adjustment for design variables with different sensitivities. Finally, motor performance (output torque, torque ripple, airgap flux density, vibration, noise) is compared pre- and post-optimization in both traditional Taguchi and the improved Taguchi-based schemes. This validation confirms the rationality and effectiveness of the proposed optimization methodology.

Keywords: permanent magnet synchronous motor, multi-objective optimization, fuzzy theory, Taguchi method, vibration noise

1. Introduction

Permanent magnet synchronous motors (PMSM) are widely used in industrial drives, new energy vehicles, and aerospace applications. Therefore, optimizing the vibration characteristics of the PMSM while ensuring its output performance is of great significance in improving the comprehensive performance of UAVs [1]. Compared with the built-in permanent magnet synchronous motor, the surface-mounted permanent magnet synchronous motor has the advantages of superior electromagnetic vibration performance, minor torque fluctuation, low-temperature rise, etc. [2].

However, a poorly designed surface-mounted permanent magnet synchronous motor will still have the problem of poor vibration performance, which will significantly affect the overall performance of the motor. Accurate and convenient analysis methods for magnetic fields and reasonable and efficient optimization methods are the key to solving the above problems. The causes of permanent magnet synchronous motor vibration can be divided into three aspects: mechanical vibration noise, fluid vibration noise, and electromagnetic vibration noise [3]. Compared with electromagnetic vibration noise, the first two types of vibration noise have less impact and can not be eliminated, so this paper does not consider it.

Electromagnetic vibration noise is the primary source of motor vibration noise, and an accurate magnetic field analysis method is the key to studying electromagnetic vibration. For permanent magnet synchronous motors, due to the magnetic saturation phenomenon, complex boundary conditions, and other factors, it is not easy to realize the accurate analysis of the magnetic field. Many scholars have proposed corresponding programs to address

©The Korean Magnetics Society. All rights reserved.

*Corresponding author:

e-mail: gczhang@cauc.edu.cn

this problem. Aiming at the shortcomings of the existing analytical calculation of electromagnetic force waves, which can not take into account the rapidity and accuracy, Xing Zezhi proposes a calculation method combining the sub-domain method and the magnetic potentialpermittivity method, which improves the efficiency of the calculation of electromagnetic force wave as well as electromagnetic vibration [4]. Chao Yang Rui derived the expression of radial electromagnetic force for a permanent magnet synchronous motor with fractional slotted concentrated winding by using the magnetic potential permeability method, taking into account the effects of stator slotting and rotor camming, and summarized the temporal and spatial orders of the electromagnetic force wave [5]. Yang et al. analyzed the distribution and change of radial electromagnetic force by Maxwell's stress method, and the change of radial electromagnetic force over time and space was obtained by [6]. Su Wu et al. analyzed the radial electromagnetic force wave of a staggered-pole hybrid excitation generator. They summarized the change rule of radial electromagnetic force wave along the axial direction of the generator [7]. However, in the process of analytical calculation of magnetic field, different calculation methods will always simplify the model to various degrees and assumptions, and these simplifications and assumptions will have an impact on the accuracy of the analytical model [8]. Consequently, solutions derived from simplified analytical models necessitate validation against corresponding finite element analyses to ensure theoretical model reliability.

In recent years, the prosperity of cross-disciplines has had a significant impact on the field of industrial design. Many optimization models based on mathematicalphysical methods, such as neural networks, genetic algorithms, and so on, have appeared. While these methods are widely used in the field of industrial design, they are also highly labor-intensive [9, 10]. Taguchi's method has attracted much attention as a solution that can achieve efficient multi-objective optimization. However, the reasonableness of the optimization results needs to be more credible due to the neglect of the influence relationship between the optimization objectives in the optimization process [11-13]. Therefore, it is necessary to select a suitable method to improve the traditional Taguchi design method for the feasibility and practicality of the overall multi-objective optimization.

Aiming at the above problems, this paper takes an 8-pole and 12-slot surface-mounted permanent magnet synchronous motor for the uncrewed aerial vehicle as the research object, studies the radial electromagnetic force wave, which is the main factor causing the vibration of

the motor, and proposes a multi-objective optimization design of the motor structure by combining with the fuzzy theory and the improved Taguchi design method. Section II establishes the finite element model of the motor, solves the spatial order distribution of the radial electromagnetic force, and compares the results with the theoretical model in Section I to verify the accuracy of the theoretical model and finite element simulation in this paper. In Section III, the Box-Behnken method is used to establish the response surface methodology (RSM) surface model between the design variables and the optimization objective and to solve the specific analytical relationship between the design variables and the optimization objective [14]. Then, an improved Taguchi method combined with the fuzzy theory is proposed to carry out the multi-objective optimization design for the electric motor structure to determine the values of the design variables. Then, a modified Taguchi method combined with fuzzy theory is proposed to optimize the design of the motor structure with multiple objectives, and the values of design variables are determined. Finally, a sensitivity analysis of each design variable is carried out based on Pearson's coefficient. Different parameter adjustment methods are adopted for the design variables with different sensitivities. Method to determine the final values of each design variable [15]. In section 4, finite element simulation of the motor model before and after optimization is carried out to verify the reasonableness and validity of the optimization method proposed in this paper by comparing the comprehensive performance of the motor before optimization, after optimization by traditional Taguchi method and after optimization by the improved Taguchi method, including the motor output performance, vibration, and noise characteristics as well as the air-gap magnetism.

2. Analysis of Electromagnetic Excitation Force Considering Tangential Electromagnetic Force

Electromagnetic force fluctuation is the primary excitation source that causes permanent magnet synchronous motor vibration, and it is necessary to analyze it comprehensively due to its complex harmonic components. Electromagnetic force fluctuation can be divided into two kinds: radial and tangential. At present, the mainstream research direction mainly adopts the one-dimensional magnetic potential permeability method. It centers around the radial electromagnetic force fluctuation, which is regarded as the leading cause of the vibration noise of the motor. In contrast, research on tangential electromagnetic

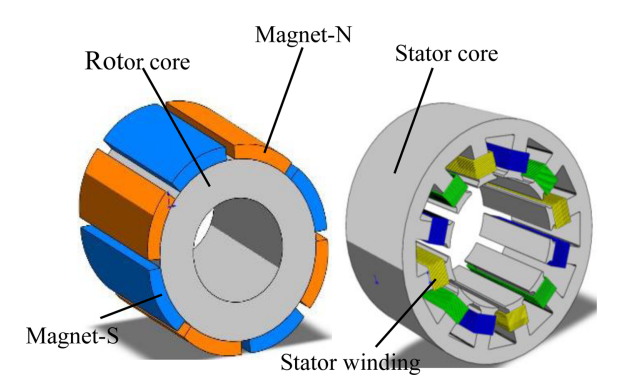


Fig. 1. (Color online) 8-pole 12-slot surface-mounted perma.

Table 1. Parameters of 8-pole 12-slot surface-mounted permanent magnet synchronous motor.

Synbol	Item	Value(unit)	
R_{s1}/R_{s2}	Outer/Inter diameter of stator core	100/53 (mm)	
R_{r1}/R_{r2}	Outer/Inter diameter of rotor core	51/25 (mm)	
L_{ef}	Effective length of motor	60 (mm)	
P	Number of pole pairs	4	
f	Frequency	200 (Hz)	
T_n	Rated torque	20.161 (N*m)	
P_n	Rated power	1000(W)	
N_n	Rated speed	3000(rpm/min)	
$\alpha_{\rm c}$	Pole arc coefficient	0.8	

force fluctuation is rare. In order to establish a comprehensive and accurate theoretical analytical model, two kinds of electromagnetic force fluctuations are investigated simultaneously in this section, and the expressions of both are rigorously deduced to provide an excellent theoretical basis for finite element analysis and multi-objective optimization design in the subsequent chapters [4].

Fig. 1 shows the structural sketch of an 8-pole, 12-slot permanent magnet synchronous motor for UAVs studied in this paper. The specific structural parameters of the motor are shown in Table 1.

2.1. Airborne air gap magnetic field analysis

To solve the expression of the air-gap magnetic field of the surface-mounted permanent magnet synchronous motor, the motor model can be simplified by first disregarding the stator slotting case. Then, the expression of the two-dimensional magnetic field under the simplified condition can be obtained. Finally, the effect of the stator slotting can be considered by introducing the relative permeability function [16, 17].

Fig. 2 shows the schematic structure of the motor with

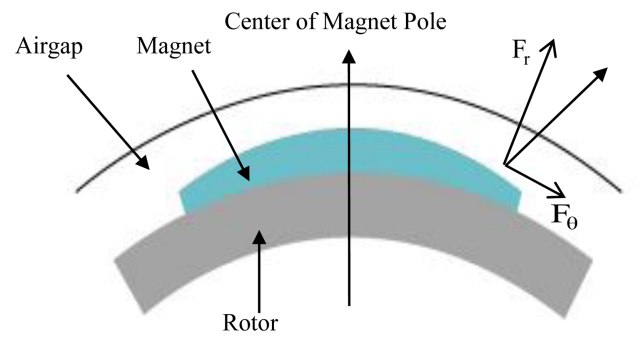


Fig. 2. (Color online) Slotless structure of surface-mounted permanent magnet synchronous motor.

a slotless structure. The no-load air gap magnetic field in the slotless case can be expressed as equation (1), where r denotes the radial and tangential directions, respectively.

$$B_{r_{PM}}(\theta, r, t) = \sum_{n=1,3,5,\cdots}^{\infty} B_{rn}^{PM}(r) \cos n(p\theta - \omega_e t)$$

$$B_{\theta_{PM}}(\theta, r, t) = \sum_{n=1,3,5,\cdots}^{\infty} B_{\theta n}^{PM}(r) \sin n(p\theta - \omega_e t)$$
(1)

Where: ω_e – electrical angular frequency; t – time

Further, the relative permeability function is introduced to consider the effect of stator slotting. The motor slotted structure is schematically shown in Fig. 3. The real and imaginary parts of the relative air gap permeability function can be expressed as Eq. (2), where is the number of stator slots. The final expression for the unloaded air gap magnetic field is further obtained as Eq. (3)

$$\lambda_{a} = \lambda_{0} + \sum_{i=1}^{\infty} \lambda_{ai} \cos(iN_{s}\theta)$$

$$\lambda_{b} = \sum_{i=1}^{\infty} \lambda_{bi} \sin(iN_{s}\theta)$$
(2)

Where N_s – Number of stator slots; $\lambda_a \lambda_b$ – Number of stator slots.

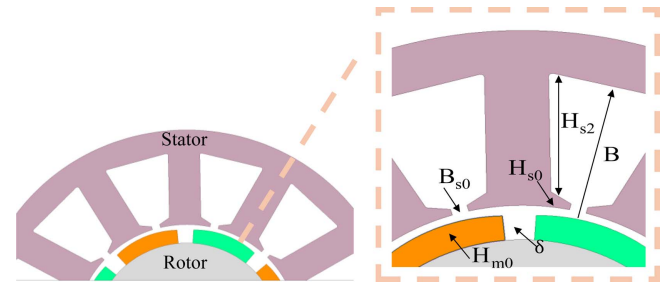


Fig. 3. (Color online) Slotted structure of surface-mounted permanent magnet synchronous motor.

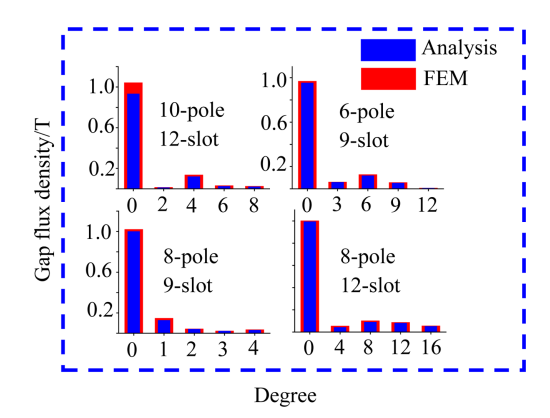


Fig. 4. (Color online) Comparison of theoretical analysis and finite element results of no-load radial air gap flux density.

$$B_{Sr_{PM}}(r,\theta,t) = \sum_{n=1,3,5\cdots}^{\infty} \sum_{i=0}^{\infty} B_{rmi}^{PM}(r)$$

$$\cos\left[(np \pm iN_s)\theta - n\omega_e t + L\right]$$

$$B_{S\theta_{PM}}(r,\theta,t) = \sum_{n=1,3,5\cdots}^{\infty} \sum_{i=0}^{\infty} B_{\theta ni}^{PM}(r)$$

$$\sin\left[(np \pm iN_s)\theta - n\omega_e t + L\right]$$
(3)

To verify the correctness of the theoretical analysis in this paper, 10-pole 12-slot, 6-pole 9-slot, 8-pole 9-slot, and 8-pole 12-slot surface-mounted permanent magnet synchronous motors are selected for the simulation of noload radial air-gap magnetism, respectively. Moreover, the finite element analysis results of air gap magnetism and theoretical analysis results are decomposed by FFT. The comparison between the two is shown in Fig. 4.

2.2. Airborne EMF analysis

From the Maxwell stress tensor method, the tangential flux density component is considered to calculate the air gap electromagnetic force wave. Considering the complexity of the results, only the radial and tangential force

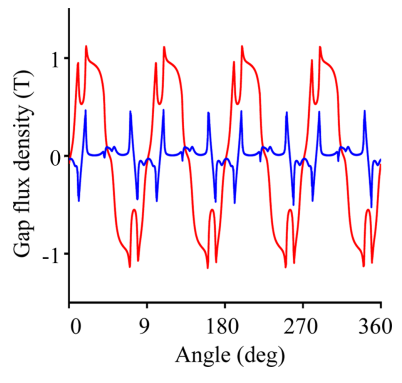


Fig. 5. (Color online) Waveforms of radial and tangential electromagnetic force under no load.

waves under no-load conditions are studied in this paper, and the rest of the working conditions are studied similarly.

Substituting Eq. (3) into Maxwell's stress tensor equation and neglecting the square term of the tangential magnetic density in the equation to facilitate calculation, we obtain the expression (4) for the radial and tangential EMF waves under no-load conditions.

$$\sigma(r,\theta,t) = \sum_{n_1} \sum_{n_2} \sum_{i_1} \sum_{i_2} \sigma_{vu}(r) \\ -(n_1 \pm n_2) p + (i_1 \pm i_2) N_s] \theta \\ -(n_1 \pm n_2) \omega_e t + \cdots \}$$

$$\tau(r,\theta,t) = \sum_{n_1} \sum_{n_2} \sum_{i_2} \sum_{i_2} \sum_{i_3} \sin\{[(n_1 \pm n_2) p + (i_1 \pm i_2) N_s] \theta \\ -(n_1 \pm n_2) \omega_e t + \cdots \}$$

$$(4)$$

To through the Maxwell software to solve the no-load radial electromagnetic force fluctuation and tangential electromagnetic force fluctuation waveforms of an 8-pole, 12-slot permanent magnet synchronous motor, the results are shown in Fig. 5. It can be seen that the overall amplitude of tangential electromagnetic fluctuation is smaller than that of radial electromagnetic force fluctuation. However, it still occupies a portion of the weight. If the motor performance requirements are high, they should be considered in light of the actual situation.

2.3. Spatial order analysis of radial electromagnetic force in fractional slot winding motors

In this paper, a fractional slot winding motor is taken as the research object, and the radial electromagnetic force is used as an example to study its spatially ordered distribution. The analysis method for the tangential electromagnetic force is similar. According to the relevant electromagnetic theory [18, 19], the number of slots per pole and phase of a permanent magnet synchronous motor can be expressed as (5)

$$q = \frac{Z}{2mp} \tag{5}$$

Where z is the number of stator slots, m is the number of motor phases, and p is the number of motor pole pairs.

The stator magnetic field harmonic magnetomotive force order and rotor magnetic field harmonic magnetomotive force order are, respectively, (6)

$$v = \left(6\frac{k}{2} + 1\right)4 = 4(3k + 1)$$

$$\mu = (2r + 1)p = 4(2r + 1)$$
(6)

Where $r = 0, 1, 2, 3 \dots, k = \pm 1, \pm 2, \pm 3 \dots$

Table 2. Spatial order analysis of radial.

			μ		
V	4	12	20	28	36
4	0				
-8	-4	4			
16		-4	4		
-20			0		
28				0	
-32				-4	4

Based on the above theory, the spatial order and frequency characteristics of the electromagnetic excitation force generated by the interaction between the permanent magnet's magnetic field and the armature's magnetic field can be deduced. In this paper, we mainly focus on the low-order electromagnetic force with large amplitude, and the results are shown in Table 2. where v is the order of the magnetic potential of the permanent magnet and μ is the order of the magnetic potential of the armature. The term with a negative sign indicates that the electromagnetic excitation force rotates in the direction opposite to that of the main pole magnetic field. The results show that the spatial orders of the electromagnetic excitation force are all integer multiples of 4 [20], which is in line with the relevant electromagnetic theory.

3. Vibration and Noise Characterization and Finite Element Simulation Verification

3.1. Radial electromagnetic force order analysis

Based on Maxwell's finite element analysis of the fluctuation of the radial electromagnetic force of an 8-pole, 12-slot surface-mounted permanent magnet synchronous motor, the air gap magnetic density under no-

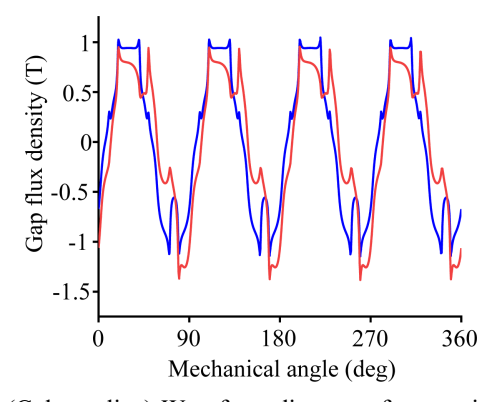


Fig. 6. (Color online) Waveform diagram of magnetic density of air gap under no-load - load condition.

load and load conditions is solved separately. The waveform of the air gap magnetic density is shown in Fig. 6. Further analysis of the vibration and noise characteristics of the motor was conducted. Since the fluctuation of the radial electromagnetic force is the main factor causing electromagnetic vibration in the motor, excessive vibration will generate loud noise during operation, seriously affecting the motor's overall performance and user experience. Therefore, to explore the vibration and noise characteristics of the motor, it is necessary to analyse and solve the fluctuation of the radial electromagnetic force.

To get the analytical relationship of electromagnetic force waves about space and time, the simulation time is set as 15 ms, the step size is 0.05 ms, and the relationship graph of radial electromagnetic force wave about space mechanical angle and time is obtained. The results are imported into MATLAB, and two-dimensional Fourier decomposition is performed. The results are shown in Figs. 7~8.

From the two-dimensional Fourier decomposition results, it can be seen that the spatial order of the radial

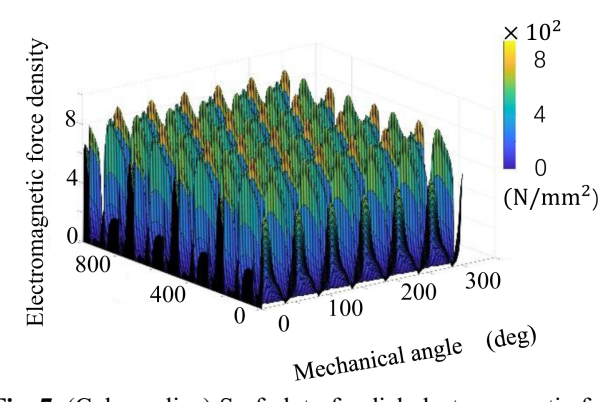


Fig. 7. (Color online) Surf plot of radial electromagnetic force density with respect to time and space.

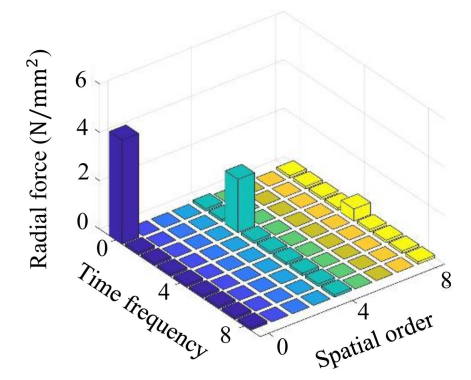


Fig. 8. (Color online) 2D Fourier decomposition of radial electromagnetic force wave.

electromagnetic force wave mainly occurs in the integer multiples of the fourth order, which is in complete agreement with the theoretical analysis results and verifies the correctness of the theoretical analysis process in this paper.

3.2. Motor Multi-Speed Vibration Characterization and Noise Simulation

Based on the workbench environment to simulate and analyze the vibration characteristics of the outer surface of the motor casing under the rated speed, the results are shown in Fig. 9.

The band diagram of the casing amplitude shows that, in general, the influence of the excitation force of the even-numbered octave frequency on the casing vibration is more prominent. The amplitude reaches a maximum value of 6.9839 Hz at 5200 Hz when the external excitation frequency is close to the casing's intrinsic frequency.

The noise characteristics of the motor at different speeds are simulated. The ERP-level waterfall diagram about the noise characteristics of the motor is obtained, as

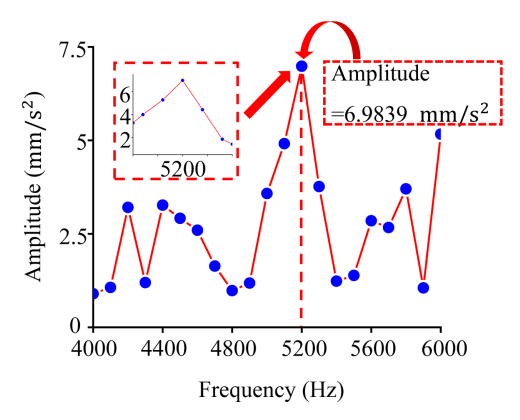


Fig. 9. (Color online) Amplitude band diagram of the casing at rated speed.

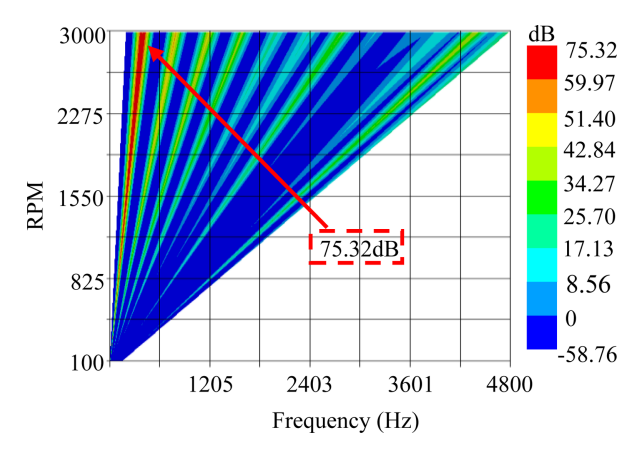


Fig. 10. (Color online) ERP waterfall of motor noise.

shown in Fig. 10. From the ERP waterfall diagram, it can be seen that when the engine operates at the rated speed, the 2-octave noise is the most significant, up to 75.32 dB. This will seriously affect the motor's performance, and it is necessary to optimise the motor's design.

4. Multi-objective Optimization Design

4.1. RSM model construction based on the Box-Behnken approach

This section uses the Box-Behnken method to construct the RSM model. The pole-arc coefficients, permanent magnet thicknesses, stator slot widths, slot edge widths, and slot depths are selected as the design variables. The optimisation objectives are used to explore the design variables for the motor output torque, torque pulsations, and load air-gap densities. Analytical relationships between these objectives and the optimal design variable ranges are established.

4.1.1. One-way experiments

A one-way experiment was conducted for each design variable to determine the relationship between the effects of each design variable on the optimisation objective. Before the experiment, the initial values of each variable were determined, and six different level values were selected for each design variable. The initial values of each variable and the selection of varying level values are shown in Table 3 (The red bolded values are the initial values of each design variable).

When a one-way experiment is conducted on a particular variable in the test, all other variables should be kept at their initial values, and the relationship between the influence of the variable to be studied on the optimisation objective should be studied by changing the variable's value. For each design variable, the experiment is conducted using the above method. The results of the experiment are shown in Fig. 11.

This study primarily focuses on the motor's output performance and its vibration/noise characteristics during operation. To enhance the motor's comprehensive performance, key performance indicators must be selected

Table 3. Initial values of single factor test.

	L_1	L_2	L ₃	L_4	L_5	L ₆
α_p	0.7	0.75	0.8	0.85	0.9	0.95
\boldsymbol{H}_{m0}/mm	3.0	3.2	3.4	3.6	3.8	4.0
$\mathrm{B}_{\mathrm{s0}}/\mathrm{mm}$	2	2.5	3	3.5	4	4.5
H_{s0}/mm	0.8	0.82	0.84	0.86	0.88	0.9
$\rm H_{s2}/mm$	14	14.5	15	15.5	16	16.5

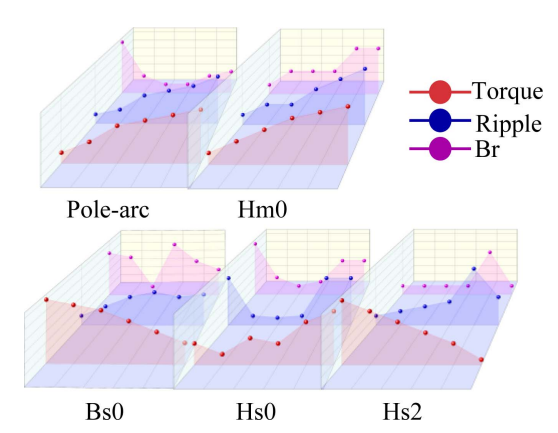


Fig. 11. (Color online) Results of the one-way test.

as optimization targets.

To improve output performance, average output torque and torque ripple are chosen as optimization objectives. This ensures high torque output while minimizing torque fluctuations, resulting in smoother power delivery. However, while increasing the load air-gap flux density can boost output torque, excessive flux density will amplify electromagnetic forces between the stator and rotor and increase harmonic components. This induces operational vibration, which may lead to bearing wear, winding loosening, structural fatigue damage, and potential detachment of surface-mounted permanent magnets. Furthermore, motor iron loss is closely related to air-gap flux density. Excessively high flux density causes iron loss to rise sharply, reducing the motor's overall efficiency.

Therefore, through optimized motor structural design, maximum average output torque and reduced torque ripple can be achieved while maintaining the load air-gap flux density within an appropriate range. This approach improves the motor's vibration characteristics during operation, avoids high iron losses, and enhances output efficiency.

To determine the analytical relationship between the optimisation objective and each variable, the response surface model of the optimisation objective concerning the design variables needs to be developed [14].

4.1.2. Response surface experiments

To determine the analytical relationship between the optimisation objective and each variable, the response surface model of the optimisation objective concerning the design variables needs to be developed [14].

For example, a response surface model is established between the average output torque and each design variable. From the initial values of each structural parameter determined in the previous section, the initial

Table 4. Significance of factors in Box-Behnken methodology.

Source	Sum of Squares	F-value	P-value
A	0.1579	0.9059	0.3515
В	0.9056	5.19	0.0327
C	0.7347	4.21	0.0522
D	0.0000	0.0002	0.9901
E	0.0003	0.0019	0.9656
AB	0.0000	0.0001	0.9914
AC	1.52	8.74	0.0073
AD	2.665e-15	1.528e-14	1.0000
AE	5.522e-06	0.0000	0.9956
BC	0.8624	4.95	0.0367
BD	8.122e-06	0.0000	0.9946
BE	2.250e-08	1.291e-07	0.9997
CD	0.0000	0.0001	0.9936
CE	2.402e-06	0.0000	0.9971
DE	6.250e-08	3.585e-07	0.9995

range of values of each design variable in the response surface experiment can be determined.

Since there are interaction and quadratic effects in the response surface model, the response surface expression used for the objective function should contain constant, linear, interaction, and quadratic terms. Therefore, the response surface expression used for the objective function in this paper is (7)

$$y(x) = a_0 + \sum_{i=1}^n a_n x_n^2 + \sum_{i=1}^n \left(\sum_{j=1}^n (a_{ij} x_i x_j) \right)$$
 (7)

Eq: a_0 denotes the intercept and denotes the quadratic effect of the denotes the interaction effect of the $i \neq j$.

Based on the Box-Behnken method, 43 experiments (including 3 at the centre point) were carried out at the initially determined range of values for the five structural parameters. The importance of each item in the results acting on the torque is analysed, and the results are shown in Table 4. When the p-value value is more significant than 0.05, it can be considered that the item does not play an essential role in the results and can be ignored. The pole arc coefficients, permanent magnet thicknesses, stator slotting dimensions, slot edge widths and slot depths are denoted by A~E, respectively.

Fig. 12 shows the average torque and pole arc factor response surface plotversus the stator slot size. As the pole arc factor and stator slot size increase simultaneously, the average motor torque gradually increases. When the stator slot size is between 3.60 mm and 3.80 mm and the pole arc factor is between 0.80 and 0.85, the average

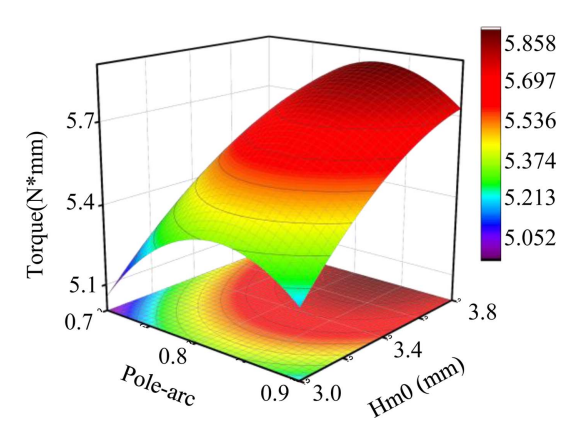


Fig. 12. (Color online) Average torque response surface diagram.

Table 5. Values of each parameter under different optimization objectives.

-	Pole-arc	H _{m0} /mm	H _{s0} /mm	B _{s0} /mm	B _{s2} /mm
Torque-Max	0.78	3.97	3.76	0.88	14.81
Ripple-Min	0.73	3.54	3.98	0.86	14.62
Br-Min	0.72	3.72	3.88	0.81	14.89

output torque of the motor shows a rapid jump. The values of each structural parameter at the maximum torque predicted by the above model are further used. Similarly, the expressions of the response surface and the response surface map of torque ripple and load air gap flux density concerning each optimised parameter are obtained and will not be repeated here. The values of each optimised parameter at the maximum output torque, minimum torque ripple and minimum load air gap flux density are shown in Table 5.

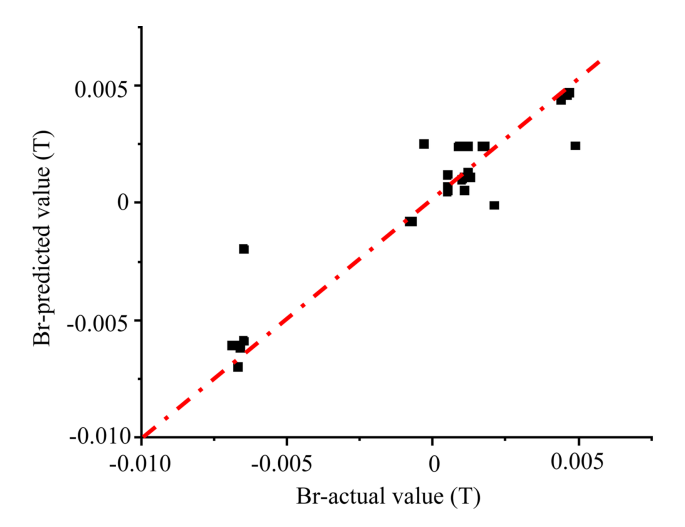


Fig. 13. (Color online) Plot of average torque residual analysis.

4.1.3. Residual analysis

In mathematical statistics, the difference between the actual observed and estimated values is referred to as the residual. In this paper, the reliability of the established response surface fitting equation is verified by performing residual analysis.

Fig. 13 shows the average torque residual analysis. As can be seen from the results of residual diagnosis, each sample point fluctuates around a straight line. This indicates that there is some linear relationship or linear movement trend between the groups of experimental data, which proves that the response surface model established in this paper has a high degree of fit with the actual three-dimensional model.

4.2. Optimized design of Taguchi method combined with fuzzy theory

The Taguchi method, proposed by Dr. Koichi Taguchi of Japan in 1952, has been widely adopted in industrial manufacturing to enhance product quality and identify optimal performance parameters. However, when three or more design variables are involved, the computational burden becomes prohibitive due to significant variable interactions. To address this limitation, this paper enhances the traditional Taguchi method by integrating fuzzy theory. The improved optimization design process proceeds as follows:

First, relevant design variables are determined based on the selected optimization objectives. Next, an orthogonal array is constructed using these variables, and finite-element simulation is employed to evaluate the performance corresponding to each experimental combination within the array. The signal-to-noise ratio (SNR) for each optimization objective is then calculated to determine the desirability score index (DSI) for each test run. Subsequently, leveraging fuzzy theory, a Multi-Performance Characteristic Index (MPCI) is computed to assess the influence of each design variable on each optimization objective.

By introducing the MPCI and incorporating adjustable weighting coefficients for the optimization objectives, the original multi-objective problem is transformed into a single-objective collaborative optimization framework. This approach allows the relative importance of each objective to be flexibly prioritized according to practical requirements. Consequently, the proposed method ensures effective optimization outcomes while significantly improving design efficiency and enhancing the applicability of the methodology.

Fig. 14 shows the improved optimisation process. When the three optimisation objectives achieve the

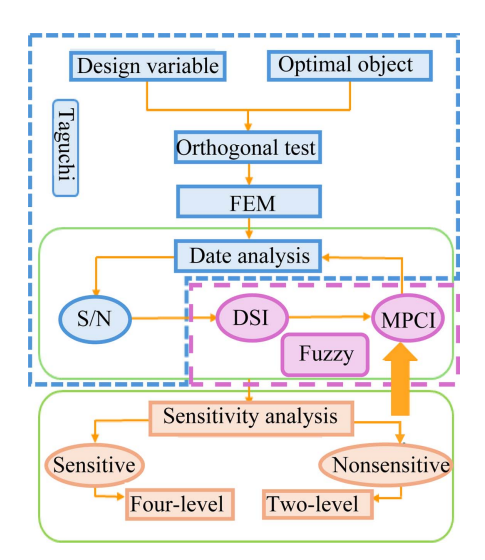


Fig. 14. (Color online) Flowchart of Taguchi method design combining fuzzy theory.

Table 6. Values of optimization factors.

	-			
Factor	L1	L2	L3	L4
α_p	0.72	0.74	0.76	0.78
H_{m0}/mm	3.54	3.62	3.70	3.78
$\mathrm{B}_{\mathrm{s0}}/\mathrm{mm}$	3.76	3.83	3.90	3.97
H_{s0}/mm	0.81	0.83	0.85	0.87
$\rm H_{s2}/mm$	14.62	14.71	14.80	14.89

optimal values in the previous section, the initial value range of each design variable in this section can be further determined based on the value of each corresponding design variable [6]. The specific values of each design variable are shown in Table 6. According to the principles of the Taguchi method, an orthogonal table is established for multi-objective optimisation to find the optimal combination of structures.

4.3. Calculation of Signal-to-Noise Ratio and DSI Values

To improve the motor's overall performance, increasing the average output torque while minimising the torque fluctuations and the load air gap magnetism [21, 22].

Based on the results of the orthogonal table test in the previous section, the signal-to-noise ratios of the three optimisation objectives are calculated [23]. Taking the average torque as an example, the signal-to-noise ratio is calculated as (8)

$$SNR\left(T_{avg}\right) = -10 \times \lg\left[\frac{1}{n} \sum_{j=1}^{n} \left(T_{avgj}\right)^{-2}\right]$$
 (8)

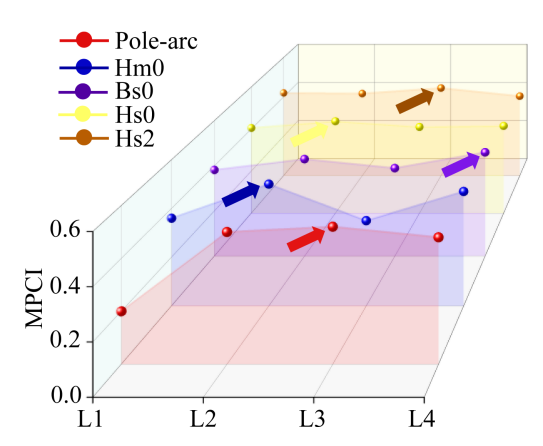


Fig. 15. (Color online) MPCI analysis results.

After calculating the signal-to-noise ratio of each group of optimisation variables, the DSI value corresponding to each group of optimisation objectives can be found according to the following formula. Taking the average output torque as an example, the DSI value of the jth torque value is calculated as (9)

$$DSI(T_{avgj}) = \frac{SNR(T_{avgj}) - \min SNR(T_{avg})}{\max SNR(T_{avg}) - \min SNR(T_{avg})}$$
(9)

A fuzzy theory processing method is further introduced to calculate the MPCI value of each data set. The MPCI value of the jth data set is calculated as follows (10)

$$MPCI_{j} = \lambda_{1}DSI(T_{avg_{j}}) + \lambda_{2}DSI(T_{rip_{j}}) + \lambda_{3}DSI(B_{r_{j}})$$

$$(10)$$

 $\lambda_1.\lambda_2.\lambda_3$ denote the weight of each optimisation objective in the overall optimisation design, respectively. Taking the level 1 design variable, For example, its MPCI value is calculated as (11)

$$MPCl(\alpha_{pl}) = \frac{1}{8} \begin{pmatrix} MPCl_1 + MPCl_2 + MPCl_3 \\ +MPCl_4 + MPCl_5 + MPCl_6 \\ +MPCl_7 + MPCl_8 \end{pmatrix}$$
(11)

The results of MPCI analysis for each design variable are shown in Fig. 15, and from the results of the analysis, it is clear that the best combination is A3, B2, C4, D2, E3

4.4. Multivariate sensitivity analysis

In optimal design, the more sensitive design variables require more detailed attention. In contrast, the less sensitive design variables can be simplified to a certain extent to streamline the design process reasonably. This

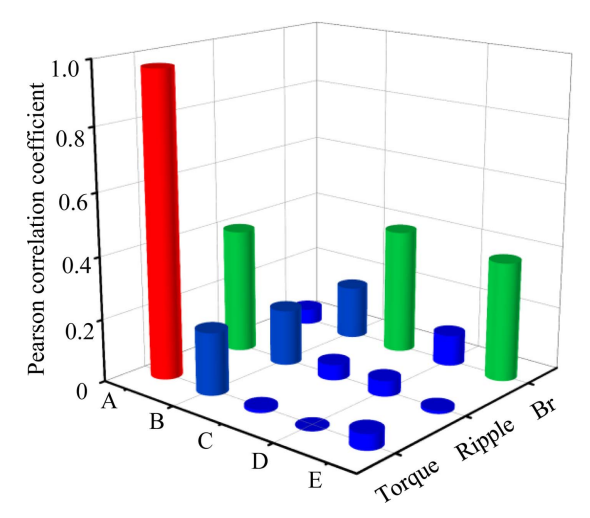


Fig. 16. (Color online) Sensitivity analysis of design variables based on Pearson's coefficients.

paper selects the Pearson coefficient to reflect the design variables.

The degree of sensitivity is calculated. The formula is shown in equation (12). Where m represents the total number of samples and represents the design variables of each group and the corresponding optimisation objectives, respectively, and the Pearson coefficient of each group of data is calculated in Fig. 16. The analysis results show that design variables A and B have high sensitivity to the optimisation objective and should be given extra attention during the design process. c,d and e have low sensitivity to the optimisation objective. For the sensitivity intensity, different design variables are selected for further design.

$$r_{xy} = \frac{m\sum x_{i}y_{i} - \sum x_{i}\sum y_{i}}{\left\{ \left[m\sum x_{i}^{2} - \left(\sum x_{i}\right)^{2} \right] \left[m\sum y_{i}^{2} - \left(\sum y_{i}\right)^{2} \right] \right\}^{\frac{1}{2}}}$$
(12)

4.5. Parameterization of design variables based on sensitivity indicators

To further approach the optimum values of the design variables, it is necessary to perform secondary refinement of each variable. This process refines the intervals between the different levels of each variable. To enhance design efficiency and focus the design process, key indicators should be selected to systematically evaluate the significance of each design variable. Secondary refinement methods can then be tailored accordingly, depending on the assessed importance of each variable.

This section makes further parameter adjustments to each design variable using sensitivity as an indicator. For design variables with high sensitivity, the original value

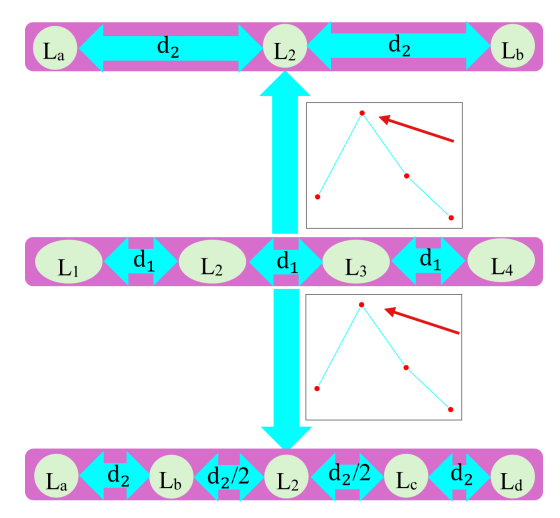


Fig. 17. (Color online) Schematic diagram of parameter adjustment for different sensitivity variables.

Table 7. Final optimized values.

$\alpha_{\rm p}$	H_{m0}	B_{s0}	H_{s0}	H_{s2}
0.765	3.605 mm	3.975 mm	0.845 mm	14.72 mm

range needs to be further refined to determine each design variable's value when the motor's overall performance is optimal. The number of test groups can be appropriately reduced for low-sensitivity design variables, simplifying the overall optimisation process. As can be seen from the sensitivity analysis results based on the Pearson coefficient in the previous section, design variables A and B are sensitive variables. In contrast, the remaining design variables are non-sensitive variables. The treatment methods for sensitive and non-sensitive variables are shown in Fig. 17.

After parameter adjustment of each design variable according to its sensitivity, the MPCI values of each design variable are recalculated. The calculation method is shown in the previous section, and the final results after optimisation are shown in Table 7.

5. Comprehensive Motor Performance Comparison before and after Optimization

The main comparison is the output performance, electromagnetic performance and vibration characteristics of the motor before and after optimization. The values of each parameter are shown in Table 8 and the results of the loss analysis are shown in Table 9. The simulation results are shown in Figs. 18-23.

Compared with the pre-optimization and the traditional Taguchi method, in terms of output performance, the

Table 8. Comparison of the values of each design variable in different methods.

Factor	Original	Traditional Taguchi	Improved Taguchi
α_p	0.8	0.875	0.765
$H_{\rm m0}/{\rm mm}$	3.6	3.625	3.605
$\mathrm{B}_{\mathrm{s0}}/\mathrm{mm}$	2	3.6	3.975
H_{s0}/mm	0.8	0.82	0.845
H_{s2}/mm	15	14.4	14.72

Table 9. The loss results before and after different optimization methods.

T£1	Before	Traditional	Improved
Type of loss	optimization	Taguchi	Taguchi
Iron loss (W)	21.94	20.16	20.6
Eddy current loss (W)	7.53	6.86	6.98

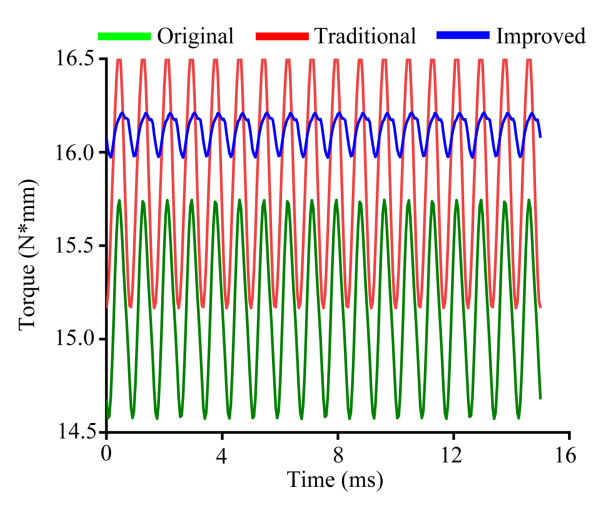


Fig. 18. (Color online) Comparison of output performance before and after optimization.

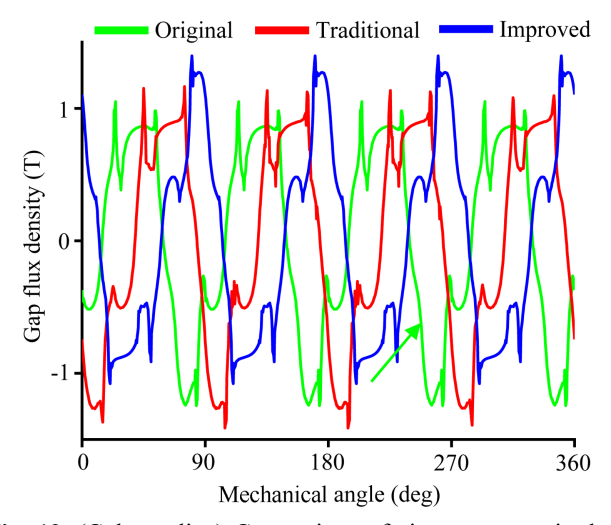
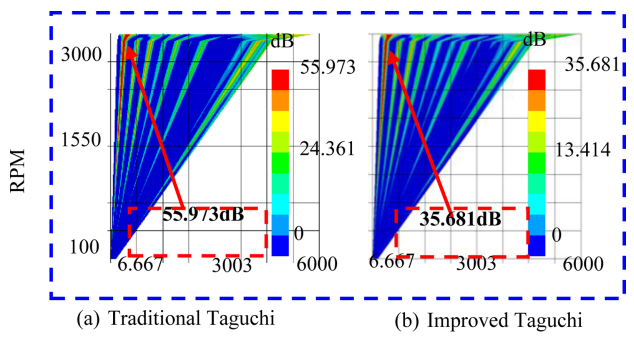


Fig. 19. (Color online) Comparison of air gap magnetic density before and after optimization.



Frequency (Hz)

Fig. 20. (Color online) Comparison of noise amplitude between traditional Taguchi method and improved Taguchi method.

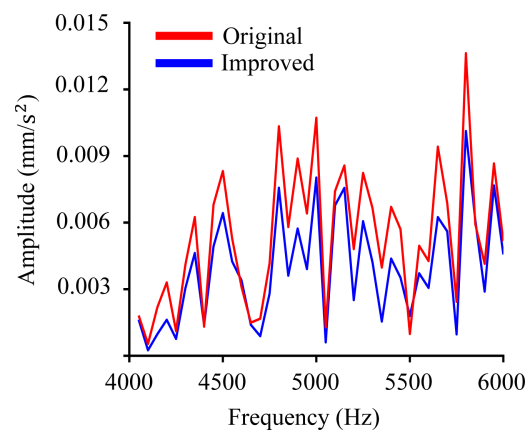


Fig. 21. (Color online) Comparison of vibration amplitude between traditional Taguchi method and improved Taguchi method.

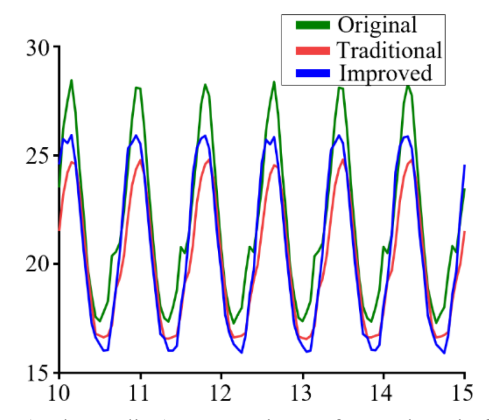


Fig. 22. (Color online) Comparison of core loss before and after different optimization methods.

design method proposed in this paper has achieved an improvement in the guaranteed average output torque from 15.1538 N*mm before optimisation to 16.1176 N*mm (the average torque of the traditional Taguchi method optimisation group average torque is 15.8567N*

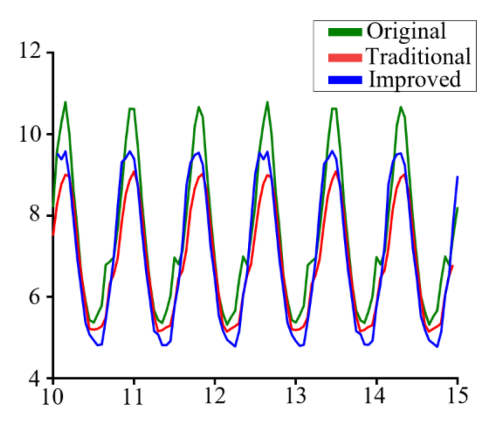


Fig. 23. (Color online) Comparison of eddy current loss before and after different optimization methods.

mm), and the torque ripple is significantly reduced, from 3.86% before optimisation to 0.75% (the torque ripple of the traditional Taguchi method optimisation group is 0.44%). In terms of air gap magnetic density, the load air gap magnetic density has also been significantly reduced. The amplitude of the load air gap magnetic density has been reduced from the original 1.3966T to 1.0514T, a reduction of up to 24.72%, and the local magnetic density changes are also smoother. In terms of vibration characteristics, compared with the traditional Taguchi method, the vibration deformation of the motor stator shell under the action of excitation forces at high, medium and low frequencies is significantly reduced. The average amplitude is reduced from to, a reduction of up to 26.4%; the maximum amplitude is reduced from to, a decrease of 25.74%. The noise level at rated speed was reduced from 75.32 dB to 35.681 dB, a reduction of 36.25%, which is significant for the motor to maintain high efficiency and good performance when operating under complex conditions. A comparison of pre- and post-optimization results using the improved Taguchi method proposed in this study reveals a discernible reduction in motor losses. Specifically, iron loss decreased from 21.94 W to 20.6 W, representing a reduction of 6.1%, while eddy current loss declined from 7.53 W to 6.98 W, a reduction of 7.3%. Compared to the conventional Taguchi method, the proposed approach exhibits a marginal increase in total losses; however, this increase is negligible. Notably, these outcomes are achieved while simultaneously delivering higher output torque, lower torque fluctuation, and improved vibration and noise characteristics.

6. Conclusion

In this paper, a theoretical, analytical model of electromagnetic force considering tangential electromagnetic

force is proposed, and the analytical model proposed in this paper is proved to be highly reliable by comparing it with finite element simulation. The mechanism of motor vibration caused by electromagnetic force fluctuation is analysed, and the vibration and noise situation of the motor under multi-speed conditions is simulated, which provides a specific thesis basis for the subsequent related research on the NVH performance of the engine. An improved Taguchi design method combined with fuzzy theory is proposed, which transforms the original multiobjective optimisation problem into a single-objective collaborative optimisation problem relative to the traditional Taguchi method and dramatically reduces the design cost while improving the optimisation effect, which is of great guiding significance for the subsequent optimisation design of other kinds of motors.

Acknowledgment

This research was supported by the Graduate Research Innovation Project of Civil Aviation University of China (2024YJSKC01013).

References

- [1] D. Liu, C. Zhan, F. Qu, L. Chen, and H. Shi, Transactions of China Electrotechnical Society **39**, 1749 (2024).
- [2] Z. Chen, Modeling, analysis and design of surfacemounted permanent magnet synchronous motor, Tianjin University, China (2014).
- [3] X. Qiu, S. Zhao, X. Yang, H. Yin, and Z. Li, Proceedings of the CSEE **44**, 3248 (2024).
- [4] H. Lan, Research on electromagnetic force wave and electromagnetic vibration of permanent magnet synchronous motor, Harbin Institute of Technology, China (2019).
- [5] Z. Xing, X. Wang, W. Zhao, and G. Ma, Proceedings of the CSEE **41**, 5004 (2021).
- [6] C. Yang, Ph.D. Dissertation, Analysis and suppression of electromagnetic vibration of permanent magnet synchronous motor with fractional slot centralized winding, Zhejiang University, China (2023).
- [7] Z. Yang, W. Li, Y. Gou, and T. Cai, J. Electr. Eng. Technol. **15**, 2601 (2020).
- [8] W. Su, N. Lin, X. Zhang, D. Wang, and Y. Guo, Proceedings of the CSEE **43**, 1569 (2023).
- [9] Z. Xing, Ph.D. Dissertation, Research on Fast Calculation Method of electromagnetic vibration of permanent magnet synchronous motor powered by frequency converter and its weakening measures, Shandong University, China (2023).
- [10] G. Cheng, X. Wang, D. Song, C. Wang, and Z. Cui, Journal of Mechanical Design, 1-11 (2024).
- [11] W. Mi, Small and Special Electrical Machines 52, 26

- (2024).
- [12] T. Guan, D. Liu, Z. Wen, and B. Pei, Micromotors **57**, 1 (2024).
- [13] Y. Zhang, W. Gao, Q. Shi, Q. Meng, and G. Du, Transactions of China Electrotechnical Society 38, 2637 (2023).
- [14] J. Liu and D. Zhu, Micromotors 54, 38 (2021).
- [15] H. Wang, Ph.D. Dissertation, Optimization of autogenous dynamic membrane formation in anaerobic bioreactor based on response surface method, Shandong University, China (2023).
- [16] Z. Wu and Z. Zhu, IEEE Trans. Magn. 51, 1 (2015).
- [17] L. Ma and X. Chen, Journal of Fuzhou University **52**, 198 (2024).
- [18] C. Yuan, Ph.D. Dissertation, Torque Performance and

- Electromagnetic Vibration Optimization Design of Builtin Permanent Magnet synchronous Motor, Harbin University of Science and Technology, China (2022).
- [19] X. Han, X. Zhang, L. Zhu, X. Ma, and S. Wang, Electric Machines and Control 25, 67 (2021).
- [20] Z. Song, Electric Machines and Control Application 45, 97 (2018).
- [21] S. Chen, S. Ding, S. Shen, Y. Dai, and Z. Yang, Transactions of China Electrotechnical Society 38, 1275 (2023).
- [22] N. Kapralov, M. Jamshidi Idaji, T. Stephani, A. Studenova, C. Vidaurre, T. Ros, A. Villringer, and V. Nikulin, Journal of Neural Engineering **21**, 056027 (2024).
- [23] Q. Wang, H. Luo, Z. Li, Y. Ding, and W. Xiong, Measurement 237, 115180 (2024).